batteries

MDPI

Article

Waste-PET-Derived Nitrogen-Doped Hard Carbon for Sodium-Ion Batteries: A Comparative Study

Qiran Lu, Weinan Zhao, Saeed Habibpour, Aklilu Getnet Messele, Yi He, Tizazu H. Mekonnen * and Aiping Yu *

Department of Chemical Engineering, Waterloo Institute for Nanotechnology, University of Waterloo, 200 University Avenue West, Waterloo, ON N2L 3G1, Canada
* Correspondence: tizazu.mekonnen@uwaterloo.ca (T.H.M.); aipingyu@uwaterloo.ca (A.Y.)

Abstract

Sodium-ion batteries (SIBs) are regarded as a promising alternative to lithium-ion batteries (LIBs). However, their advancement is constrained by the sluggish kinetics and modest capacity of conventional hard carbon (HC) anodes. Here, we report an upcycling strategy that transforms post-consumer polyethylene terephthalate (PET) bottles into nitrogen-doped hard carbon (NHC) through KOH-assisted pyrolysis followed by a separate urea-assisted nitrogen-doping treatment. The resulting NHC exhibits enlarged interlayer spacing and incorporates nitrogen into the carbon structure. Benefiting from this tailored architecture, the optimized NHC-800 delivers a high reversible capacity of 310.7 mAh g^{-1} at 20 mA g^{-1} over 874 cycles. Furthermore, a comparative mechanistic investigation of HC, NHC, reduced graphene oxide (rGO), and carboxyl-functionalized multi-walled carbon nanotubes (MWCNTs-COOH) reveals architecture-dependent sodium-storage pathways, ranging from intersheet diffusion in rGO and kinetically asymmetric storage in oxidized nanotubes to adsorption–intercalation–nanopore filling in hard carbons. This study not only elucidates the principles of rational defect and spacing engineering for developing high-performance SIB anodes but also demonstrates a strategy to upcycle plastic waste, thereby reducing the landfill burden and mitigating dependence on critical lithium resources.

Keywords: sodium-ion batteries; hard carbon; nitrogen doping; interlayer spacing; defect

1. Introduction

Lithium-ion batteries (LIBs) are widely used in portable electronics and electric vehicles, but concerns over the availability and geographical distribution of lithium resources have motivated interest in alternative energy-storage technologies [1]. Sodium-ion batteries (SIBs) are a promising option because of the abundance of sodium resources and their electrochemical similarities to LIBs [2]. Their potential cost advantages also include the use of aluminum current collectors at the anode [3]. Developing suitable anode materials remains essential to improving their energy-storage performance [4].

While these features are indeed advantageous, the transition from LIBs to SIBs is not easy. The leading anode material for LIBs, graphite, is typically inexpensive and shows exceptional cycling performance. It is, however, incompatible with sodium-ion batteries because the Na^+ ion's ionic radius is larger than that of Li^+, rendering it impossible to intercalate into the dense layers of graphite [5]. As a result, a wide range of carbonaceous materials is being researched as potential SIB anodes, including graphene, carbon nanotubes, soft carbon, and hard carbon [6,7].

The electrochemical properties of these materials are critical for practical applications and must be considered alongside their microstructural features. For instance, graphene

Check for updates

Academic Editor: Nikhil A. Koratkar

Received: 15 October 2026
Revised: 4 November 2026
Accepted: 10 November 2026
Published: 16 November 2026

Copyright: © 2026 by the authors. Licensee MDPI, Basel, Switzerland. This article is an open access article distributed under the terms and conditions of the Creative Commons Attribution (CC BY) license.

has remarkable electronic conductivity, whereas carbon nanotubes provide convenient one-dimensional channels for ion transport, but they are associated with high cost. Soft carbon tends to partially graphitize at elevated temperatures, resulting in relatively ordered carbon layers with smaller interlayer spacing, which limits Na^+ intercalation compared with the highly disordered structure of hard carbon [8,9]. In comparison, hard carbon (HC) consists of turbostratically stacked graphene layers with enlarged interlayer spacing, which aids sodium storage [10]. As a result, HC has specific capacities close to 300 $mAh \cdot g^{-1}$, which enables its use in SIBs as one of the most economically attractive anode materials, as both performance and cost targets are met [11]. Other advantages of HC include its slope- to plateau-type behavior for sodium ions originating its defects/edges and nanopores, suitable operating potential, and ease of manufacture leading to low cost. However, the lower energy density of the HC is still limiting its applications in SIBs [12].

The growing focus on waste plastics and associated environmentally friendly solutions has spurred innovation to turn them into value-added carbon materials. Plastics that are not biodegradable pose a serious environmental challenge due to their ability to break down into microplastics that absorb toxic chemicals and enter the human food chain biochemically [13]. Functional carbonaceous materials such as graphene, carbon nanotubes, carbon dots, and hard carbon can be produced through chemical recycling pathways, which involve the depolymerization of these materials into valuable precursors or direct conversion of such structures [14]. Polyethylene terephthalate (PET), which is abundant in beverage bottles, has been proven to be a carbon precursor among many other waste plastics [15,16]. As an aromatic polyester, polyethylene terephthalate (PET) is quite different from other polyolefin wastes like polypropylene and polyethylene, which makes it a potential precursor for hard carbon. This is due to its aromatic polyester structure, which comprises a large number of benzene rings and oxygen-containing ester groups. During its pyrolysis, PET tends to lose aromatic intermediates, which are needed to rearrange into turbostratic carbon domains with an interlayer spacing large enough for Na^+ to be stored at a lower potential. Also, the high oxygen content of PET is released as CO/CO_2, which is an in-situ activation step that introduces abundant micro/mesopores into the carbon framework, which enhances the pore-filling and ion transport capability [16,17]. Relating to feedstock, post-consumer PET bottles have the potential to be produced at multi-million-ton scales and collected in a highly purified, almost compositionally uniform, and low inorganic impurity form, which is beneficial in comparison to biomass or trash mixed plastic, as it allows for the production of reproducible and scalable hard carbons more easily [18,19].

The surface of a hard carbon material strongly influences its sodium storage properties. Nitrogen doping has been shown to be an effective strategy for enhancing the electrochemical properties of hard carbon anodes. The incorporation of nitrogen atoms into the carbon lattice not only improves the intrinsic electronic conductivity by introducing additional charge carriers but also creates abundant defects and heteroatomic sites that serve as active centers for Na^+ adsorption [20]. For instance, Ma et al. produced nitrogen doped hyper-crosslinked hard carbon from styrene and terephthalaldehyde, which exhibited a remarkable initial capacity of 320 $mAh \cdot g^{-1}$ with a current density of 20 $mA \cdot g^{-1}$ [21]. In addition, Song and co-workers synthesized three-dimensional N/O co-doped hard carbons using poly (aniline-co-pyrrole), which had an enlarged interlayer distance and remarkable long-term cycling stability of 69.8% capacity retention after 15,000 cycles [22]. More recently, Zhang et al. utilized a 2D self-templating technique to synthesize nitrogen-doped hard carbon from waste PET, generating mesoporous structures containing interconnected channels, which showed excellent reversible capacity of 452 $mAh \cdot g^{-1}$ at 20 $mA \cdot g^{-1}$ and was attributed to increased ion transport pathways and abundant adsorption sites [23]. Despite these advances, improvements in the electrochemical performance of nitrogen-doped hard carbon

do not, by themselves, clarify how its sodium-storage behavior differs from that of other carbon architectures. In particular, a comparison between undoped and nitrogen-doped hard carbon can identify changes associated with the modification treatment, but provides limited context for interpreting these changes relative to the storage behavior of layered and tubular carbons. A comparative investigation of PET-derived HC and NHC alongside rGO and MWCNTs-COOH under common electrochemical testing conditions is therefore needed to examine how their distinct structural characteristics relate to sodium-storage behavior and kinetics. Such a comparison can help contextualize the effects of nitrogen incorporation and the accompanying structural changes in waste-plastic-derived hard carbon.

Considering these advances, the conversion of waste plastics, particularly PET, into nitrogen-doped hard carbon offers a dual solution by simultaneously addressing sodium-ion storage and plastic waste management. By combining the structural tunability of waste-derived carbon with the defect-engineering capability of nitrogen doping, advanced anode materials can be rationally designed for next-generation sodium-ion batteries (SIBs). Herein, we develop a simple route for upcycling post-consumer PET into nitrogen-doped hard carbon through KOH-assisted carbonization and urea-mediated nitrogen incorporation. The treatment simultaneously regulates the defect population, nitrogen configuration, pseudo-graphitic interlayer spacing, and pore architecture. The optimized NHC-800 delivers a high initial charge capacity of 363 mAh g^{-1} at 20 mA g^{-1} with stability up to 85.6% over 874 cycles and demonstrates stable operation in an NHC-800//NVP full cell. To investigate how sodium-storage behavior and kinetics vary among different carbon architectures, we compare PET-derived HC and NHC with rGO and MWCNTs-COOH under the same electrochemical testing conditions. By combining structural characterization with cyclic voltammetry, kinetic analysis, galvanostatic intermittent titration, and electrochemical impedance spectroscopy, we examine differences in sodium-storage behavior and kinetics among these carbons. This comparative approach places the behavior of NHC within a broader structural context and provides insight into how nitrogen incorporation and the accompanying changes in defects, interlayer spacing, and pore structure relate to its electrochemical performance. Overall, considering battery performance, cost, and environmental protection, the upcycled NHC-800 stands out as the best candidate for practical SIB applications.

2. Experimental Section

2.1. Materials and Chemicals

Graphite was purchased at Alfa Aesar (Ward Hill, MA, USA), and multi-walled carbon nanotubes (MWCNTs) were supplied by Cheap Tubes Inc. (Grafton, MA, USA). These two chemicals were used without any purification. Used water bottles (Real Canadian Brand, Waterloo, ON, Canada) were collected and cleaned as the source of polyethylene terephthalate (PET). Potassium hydroxide (KOH) (ACS reagent grade, ≥97%), hydrochloric acid (HCl) (ACS reagent grade, 37%), urea (ACS reagent grade, ≤0.001% (Heavy Metals by ICP-OES, metals basis), 99.0–100.5%, solid), nitric acid (HNO_3) (ACS reagent, 70%), sulfuric acid (H_2SO_4) (ACS reagent, 95.0–98.0%), phosphoric acid (H_3PO_4) (ACS reagent, ≥85 wt. % in H_2O), hydrogen peroxide (H_2O_2) (30 wt. % in H_2O, ACS reagent), ethanol (anhydrous, ≥99%), dimethyl carbonate (anhydrous, ≥99%), ethylene carbonate (98%) and sodium perchlorate (≥99.9% trace metals basis) were all purchased from Sigma-Aldrich (Toronto, ON, Canada).

2.2. Synthesis of Reduced Graphene Oxide (rGO)

rGO was synthesized by an improved method [24] alongside thermal reduction. For GO production, 3.0 g of graphite, 360 mL of concentrated H_2SO_4, and 40 mL of H_3PO_4

(9:1 volume ratio) were placed in an Erlenmeyer flask on an ice bath. Then, 18.0 g of $KMnO_4$ was added slowly to the mixture. The reaction was stirred and heated to 45 °C for 16 h. Water and H_2O_2 were added to the cooled-down resultant to stop the reaction. The mixed liquid was centrifuged with hydrochloric acid, ethanol, and water. After washing, GO samples were freeze-dried to remove water content. The thermal reduction was conducted by heating GO samples at 950 °C under an Ar atmosphere.

2.3. Synthesis of Functionalized Multi-Walled Carbon Nanotubes (MWCNTs-COOH)

Typically, 24 mL HNO_3, 72 mL H_2SO_4, and 0.75 g MWCNTs were heated at 105 °C for 6 h in a round-bottom flask. The resultant was washed by centrifugation to remove remaining acid. The final product was obtained after freeze-drying.

2.4. Synthesis of Hard Carbon (HC)

The hard carbon was prepared through the method reported earlier [25]. Briefly, cleaned post-consumer PET bottle pieces were embrittled using liquid nitrogen, ground, and sieved. PET powder (1.5 g) and KOH (1.5 g) were mixed in 15 mL of water at a KOH mass ratio of 1:1. The mixture was dried at 80 °C overnight. The resulting KOH-coated PET was heated to 800 °C at 10 °C min^{-1} under a nitrogen atmosphere and held for 1 h. The carbonized product was washed with 200 mL of 1 M HCl for 1 h. Additional washing used a total of 1 L of water and 500 mL of ethanol per batch, with the solid recovered by centrifugation. After drying at 80 °C overnight, HC was obtained with a yield of approximately 40%, calculated from the dry HC mass relative to the initial PET mass.

2.5. Synthesis of Nitrogen-Doped Hard Carbons (NHC)

The nitrogen-doped hard carbon (NHC) was synthesized using a method in literature [26]. HC (0.3 g) and urea (0.9 g) were mixed at a urea mass ratio of 3:1. Under an argon atmosphere, the mixture was heated to 400 °C at 2 °C min^{-1} and held for 2 h, followed by heating to the target temperature (700, 800, or 900 °C) at 5 °C min^{-1} and holding for 3 h. Each batch was washed with 200 mL of 2 M HCl, with additional washing using a total of 1 L of water and 500 mL of ethanol. The products were then dried in a vacuum oven at 80 °C for 24 h and denoted as NHC-T, where T represents the final treatment temperature. The yield of NHC-800 was approximately 70%, calculated from the dry NHC-800 mass relative to the mass of HC used for nitrogen doping.

2.6. Material Characterization

Morphology of samples and elemental mapping were examined by a field-emission scanning electron microscopy (SEM) with energy-dispersive X-ray spectroscopy (EDS) capability (UltraPlus, Zeiss, Zurich, Switzerland). HR-TEM (LIBRA 200 MC, Zeiss, Switzerland) was employed to visualize the nanostructure of hard carbons. X-ray diffraction (XRD) measurements were conducted via a XRD machine (Miniflex 600, Rigaku, Tokyo, Japan) using Cu Kα radiation ($\lambda = 0.15406$ nm). X-ray photoelectron spectroscopy (XPS) was conducted through a PHI 5000 VersaProbe III. Raman spectra were collected using a WITec alpha300R confocal Raman microscope (532 nm laser).

Determination of Mesopore Volume and Median Pore Diameter

N_2 adsorption–desorption measurements were performed at 77 K using a Micromeritics Gemini VII 2390a gas adsorption analyzer. Before measurement, the samples were degassed under vacuum at 300 °C for 1 h. The mesoporous characteristics of the samples were evaluated from the N_2 adsorption–desorption isotherms using the BJH

(Barrett–Joyner–Halenda) method applied to the desorption branch. The mesopore volume (V_{meso}) was obtained by integrating the differential pore volume distribution (dV/dD) over the pore-diameter range of 2–50 nm, according to:

$$V_{meso} = \int_2^{50} \frac{dV}{dD} dD$$

To determine the median pore diameter (D_{50}), a cumulative pore-volume curve was constructed from the same BJH data, and (D_{50}) was defined as the pore diameter at which the cumulative volume reached 50% of the total mesopore volume [27]. These parameters provide a representative measure of the dominant mesopores within the material.

2.7. Electrode Fabrication and Electrochemical Testing

2.7.1. Electrode Fabrication

A half-cell setup (two-electrode configuration) assembled in CR2032 coin cell was employed for electrochemical performance tests [28]. A polished sodium metal plate was cut into 13 mm disks as both reference and counter electrodes. The preparation of the working electrode uses active material, acetylene black, and polyvinylidene fluoride (PVDF) at a weight ratio of 70:10:20 dissolved in an appropriate amount of N-methyl-2-pyrrolidone (NMP) [29]. The slurry was cast onto copper foil and dried in a vacuum oven at 70 °C for 12 h. The working electrodes were 13 mm in diameter, with a dry coating mass of approximately 2.0 mg per electrode, excluding the copper foil. This corresponds to an active-material mass of approximately 1.4 mg and an active-material loading of approximately 1.05 mg cm^{-2}. 1 M $NaClO_4$ in a mixture of ethylene carbonate (EC) and dimethyl carbonate (DMC) (volume ratio: 1:1) was utilized as electrolyte. Glass fiber from Whatman (GF/D) was used as the separator.

In addition to half-cell tests, a sodium-ion full cell was also assembled using NHC-800 as the anode and sodium vanadium phosphate (NVP) as the cathode with an N/P ratio of approximately 1.08–1.15 (anode/cathode capacity ratio). Before full-cell assembly, the NHC-800 anode was electrochemically presodiated by cycling against sodium metal for 100 cycles at 20 mA g^{-1} within a potential window of 0.01–2.0 V versus Na^+/Na, ending in the sodiated state. The current density was normalized to the NHC-800 active-material mass. The presodiated anode was subsequently used to assemble the NHC-800//NVP full cell. No additional activation cycles were performed after full-cell assembly. The NVP cathodes were 12 mm in diameter and contained 3.3–3.5 mg of active material per electrode, corresponding to an active-material loading of 2.92–3.09 mg cm^{-2}. Each full cell contained 120 µL of 1 M $NaClO_4$ in EC:DMC (1:1, *v*/*v*) without FEC. Both the current density and specific capacity reported for the full cells were normalized to the NHC-800 anode active-material mass, whereas the specific energy was calculated by integrating the discharge voltage–capacity curve and normalizing the resulting energy to the combined active-material mass of the cathode and anode. All coin cells were assembled in an argon-filled glove box (Mbraun, Stratham, NH, USA), where the oxygen and moisture levels were maintained below 0.5 ppm.

2.7.2. Electrochemical Testing

Galvanostatic charge–discharge tests for sodium-ion half-cells were conducted using a LAND CT2001A battery testing system (LAND, Wuhan, China) within a voltage range of 0.01–2.0 V. The full cells were tested within a voltage window of 1.5–3.7 V, consistent with a previously reported NVP/hard-carbon full-cell study [30]. Cyclic voltammetry (CV) and electrochemical impedance spectroscopy (EIS) were performed on the electrochemical station (VSP-300, Bio-Logic, Seyssinet-Pariset, France).

3. Results and Discussion

3.1. Morphological and Structural Characterization

Figure 1a describes the process of carbonization of PET and the overall synthetic pathway of nitrogen-doped hard carbon (NHC). As mentioned in the previous section, recycled PET bottles were used as the precursor, dipped in liquid nitrogen to induce brittleness, crushed, and sieved to obtain micro-sized flakes. The PET powders were then mixed with KOH and pyrolyzed in a nitrogen atmosphere to obtain pure hard carbon. During activation, KOH interacts with carbon to form H_2, CO, and CO_2, thereby sculpting and triggering micro- and mesopores on the carbon framework. Simultaneously, K_2O and K_2CO_3 produced during the activation process tend to react with carbon, thereby converting them to metallic potassium. The continuous redox cycling of K/K_2O enables repeated intercalation of metallic K into the carbon layers, expanding the interlayer spacing through a "templating expansion effect" [25]. Urea decomposition occurs within the temperature range of 400 to 800 °C, and the gaseous products can then diffuse into the carbon pores, allowing nitrogen to be incorporated into the frame [26]. The nitrogen-doping treatment is accompanied by changes in the carbon structure, as reflected in the Raman spectra and the increased apparent interlayer spacings obtained from XRD fitting. These changes cannot be attributed to nitrogen having a larger covalent radius than carbon [31]. A more plausible explanation is nitrogen-associated restructuring of the carbon framework, particularly local distortion and changes in the stacking of carbon layers. Previous studies have associated pyrrolic-N-containing structures with enlarged interlayer spacing [32]; the five-membered rings associated with pyrrolic N can introduce local strain and distort the carbon framework, thereby contributing to interlayer expansion [33]. Such configuration-dependent structural effects provide a plausible explanation for the increased apparent interlayer spacings observed here. However, the present measurements do not establish the dominant microscopic mechanism or isolate the contribution of nitrogen incorporation from that of the accompanying thermal treatment. Figure 1b schematically illustrates the structural modifications introduced by nitrogen doping and their influence on the formation of the solid electrolyte interphase (SEI). After nitrogen doping, both the specific surface area and mesopore diameter decrease slightly, reducing SEI formation during the initial discharge and contributing to an improvement in initial coulombic efficiency [34].

Figure 1c illustrates a typical sodium-ion battery (SIB) structure, which comprises a cathode and an anode separated by an ion-conducting electrolyte [35]. During charging, Na^+ ions are extracted from the cathode and transported through the electrolyte to the anode for storage. During subsequent discharge, they migrate back to the cathode, enabling reversible sodium storage in both electrodes, thus completing the electrochemical cycle and generating electrical energy. Reduced graphene oxide (rGO) and carboxyl-functionalized multi-walled carbon nanotubes (MWCNTs-COOH), previously investigated as carbon electrodes for sodium storage [6,36,37], were included to place the performance of PET-derived HC and NHC within a broader carbon-electrode context. Using a common electrode formulation and electrochemical testing protocol enables direct comparison of their sodium-storage performance under the conditions investigated. It should be noted that rGO and MWCNTs-COOH serve as comparative carbon materials rather than matched structural controls, because differences in surface chemistry, heteroatom content, and textural properties prevent the observed electrochemical differences from being attributed solely to carbon architecture. Precise insight into the fine microstructure of the carbon anodes was obtained using scanning electron microscopy (SEM), as shown in the right panel of Figure 1c. In the first picture, the reduced graphene oxide (rGO) appears as a loose stack of paper-thin, wrinkled sheets that spread out in rough, lamellar swaths a few micrometers wide. The crinkled, accordion-like morphology results in a large accessible surface area, which can

facilitate electrolyte penetration and ion transport during electrochemical reactions. Underneath the rGO is the tangled, three-dimensional web of MWCNTs-COOH. The filaments twist and intertwine, improving both electrical conductivity and electrolyte accessibility. The third image shows hard carbon (HC), consisting of jagged, brick-like particles aggregated together. These irregular chunks exhibit rough surfaces speckled with wispy carbon flakes likely formed during the high-temperature treatment, and this disorder increases the number of active sites and may affect the overall electrochemical behavior. Finally, the last picture depicts the microstructure of nitrogen-doped hard carbon (NHC). Compared with pristine hard carbon, the NHC particles appear to exhibit more fragments, indicating a hierarchical pore structure resulting from nitrogen incorporation. The unique shapes and appearances of rGO, MWCNTs-COOH, HC, and NHC highlight their intrinsic structural differences and play a critical role in determining their performance as electrode materials.

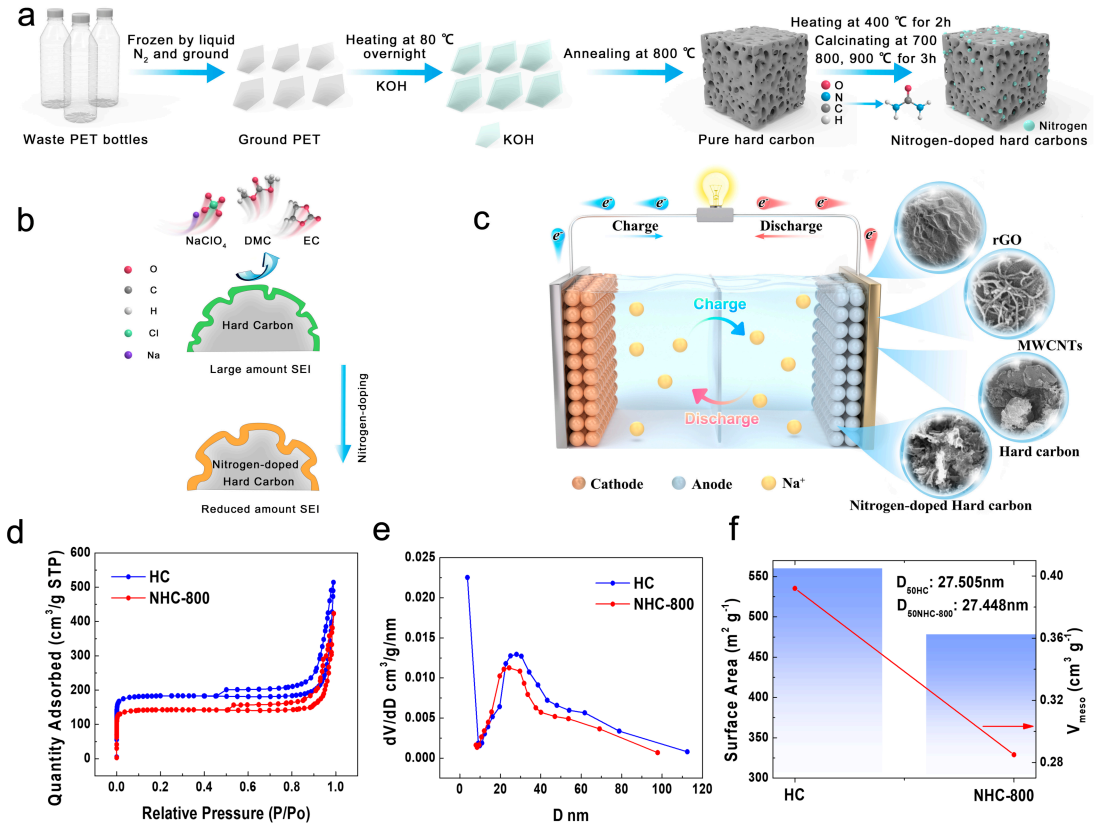


Figure 1. (**a**) Preparation route of N-doped hard carbon derived from waste PET via KOH activation and urea-assisted nitrogen incorporation; (**b**) structural evolution and SEI formation differences between pristine and nitrogen-doped hard carbon; (**c**) schematic illustration of the charge/discharge mechanism of a sodium-ion battery and comparison of carbon-based anode materials (rGO, MWCNTs, hard carbon, and nitrogen-doped hard carbon); (**d**) N_2 adsorption–desorption isotherms of hard carbons; (**e**) pore size distribution of hard carbons; (**f**) surface area, mesopore volume and median pore diameter of hard carbons.

Figure S1 presents an HRTEM image of NHC-800 and the corresponding fast Fourier transform (FFT) pattern. The imaged region exhibits short, curved carbon fringes, with some locally aligned domains but no extensive ordered stacking. The diffuse rings in the FFT pattern are consistent with limited structural coherence within this region. These observations qualitatively suggest a predominantly disordered local carbon structure with short-range ordering; however, they are insufficient to establish a turbostratic stacking arrangement.

Figure 1d,e compare NHC-800 with pristine HC using N2 adsorption–desorption isotherms and BJH pore-size distributions. Both samples show classic type-IV loops with H4-type hysteresis loops, a hallmark of slit-shaped micro-/mesopores originating from the turbostratic graphene stack [38]. The HC isotherm rises rapidly below P/P0 0.05, and exhibits a larger overall adsorption capacity, which is a sign of its porous network built by plentiful mesopores. The pore-size curve peaks sharply below 2 nm and spreads out between 15 and 40 nm. After nitrogen introduction at 800 °C, the global isotherm shifts downward, and the hysteresis loop narrows, indicating that total pore volume and specific surface area have declined. This reduction in surface area can suppress excessive SEI formation and improve the initial coulombic efficiency [39]. In Figure 1e, the micro-pore peak of NHC-800 is attenuated, the shoulder at 3–5 nm almost disappears, and the mesopore maximum is slightly shifted toward smaller diameters. These shifts imply that N incorporation and thermal treatment reconstructed the carbon walls, thereby densifying them and blocking some ultramicropores, yet leaving a hierarchical micro/mesoporous texture that facilitates Na^+ diffusion. Figure 1f compares the textural parameters of the pristine hard carbon (HC) and nitrogen-doped NHC-800, including BET surface area, mesopore volume (Vmeso), and median pore diameter (D50). The HC sample exhibits a surface area of 560.25 $m^2\ g^{-1}$ and a mesopore volume of 0.392 $cm^3\ g^{-1}$, while NHC-800 shows reduced values of 478.34 $m^2\ g^{-1}$ and 0.285 $cm^3\ g^{-1}$, respectively. Despite these significant decreases in accessible surface and mesoporous volume, the dominant mesopore size remains essentially unchanged, with D50 values of 27.505 nm (HC) and 27.448 nm (NHC-800). This indicates that nitrogen doping does not alter the characteristic pore size but instead reduces the total number of mesopores, resulting in a more compact pore network.

The evolution of carbon microstructure from pristine hard carbon (HC) to N-doped hard carbon prepared at 700, 800 and 900 °C (NHC-700, NHC-800 and NHC-900) was quantified by simultaneous Raman and X-ray diffraction (XRD) analysis. Figure 2a presents the Raman spectra of the four carbon materials. Each profile shows the characteristic pair of peaks near 1350 cm^{-1} and 1580 cm^{-1}, assigned to the defect-related D peak and the graphitic E_{2g} G peak, respectively [40]. The I_D/I_G ratios are 1.06, 1.10, 1.20, and 1.18 for HC, NHC-700, NHC-800, and NHC-900, respectively. NHC-800 exhibits the highest I_D/I_G ratio in this series. These differences indicate changes in the relative D- and G-band intensities following the modification treatment, but do not independently quantify the concentrations of specific defect types.

Detailed structural information is needed for analyzing these samples. The broad D peak in the spectrum was deconvoluted into four components by using Lorentzian equation (Figures S2–S5). The D1 sub-peak, centered at 1350 cm^{-1}, originates from A_1g breathing modes in disordered graphitic domains [41]. The D2 feature (around 1620 cm^{-1}) is attributed to defect scattering in few-layer graphene regions [42]. The D3 peak (near 1500 cm^{-1}), reflects vibrational modes of short-range sp^3-hybridized carbon within the amorphous matrix [43]. Finally, the D4 peak at 1200 cm^{-1} is attributed to stretching vibrations of heteroatom-terminated sp^2-sp^3 edge sites [43]. Together, the evolution of these sub-peaks offers a nuanced picture of how nitrogen doping modulates the balance between graphitic order, amorphous carbon, and heteroatom-functionalized edges.

As summarized in Table S1, the fitted D1 contribution increases from 53.52% to 66.54% and 71.59% for NHC-700, NHC-800, and NHC-900, respectively. In contrast, the D2 contribution reaches its maximum in NHC-700 (15.09%) and decreases to 5.74% in NHC-800 and 2.95% in NHC-900, compared with 2.63% in HC. The D4 contribution also decreases across the NHC series, from 16.07% to 13.27% and 8.40%. These values describe changes in the relative areas of the fitted Raman components rather than absolute populations of individual defects. In particular, the D2 area fraction and the I_D/I_G intensity ratio are distinct

spectral descriptors and should not be interpreted interchangeably. Thus, the highest I_D/I_G ratio in NHC-800 does not imply that this sample also has the largest D2 contribution. The Raman results reveal changes in the carbon structure with treatment temperature, while specific nitrogen configurations are examined separately by XPS.

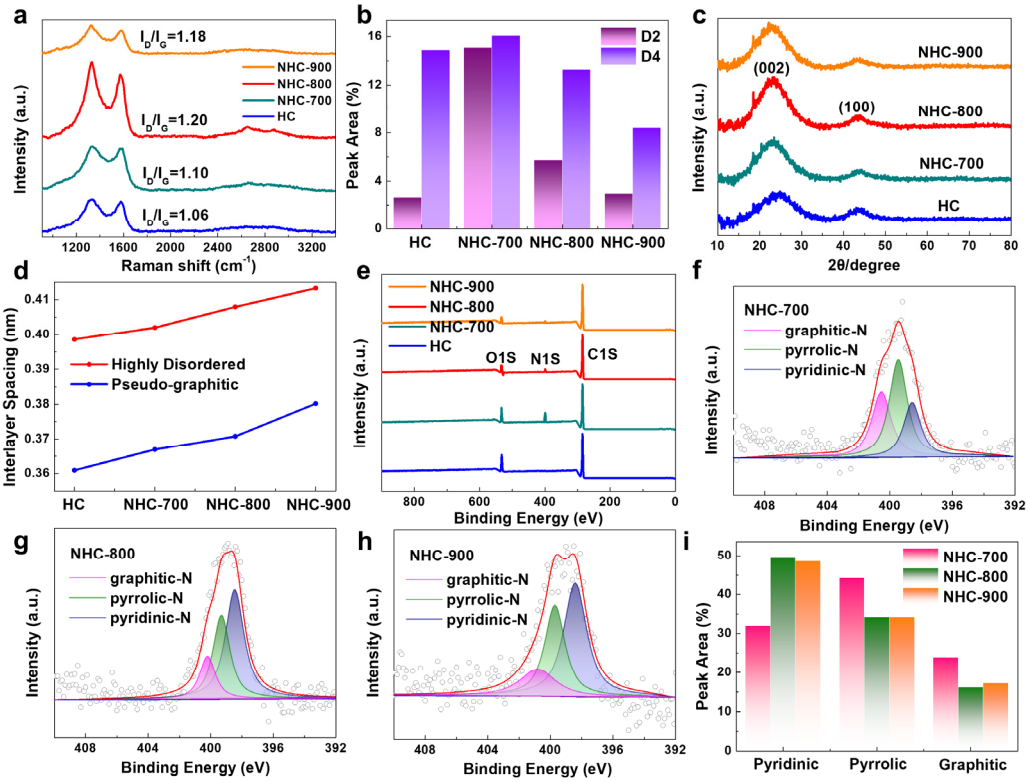


Figure 2. (**a**) Raman spectra of hard carbons; (**b**) proportion of D2 and D4 defect peaks in Raman spectra of hard carbon and N-doped hard carbons; (**c**) XRD patterns of hard carbon and N-doped hard carbons; (**d**) interlayer spacing of hard carbon and N-doped hard carbons; (**e**) XPS survey spectra of HC and NHCs; (**f**) high-resolution N 1s spectra for NHC-700; (**g**) high-resolution N 1s spectra for NHC-800; (**h**) high-resolution N 1s spectra for NHC-900; (**i**) nitrogen components in NHCs.

The Raman trends are echoed in the XRD data (Figure 2c). As shown in Figure 2c, two typical broad peaks appear at approximately 23° and 43.7° in all samples, which correspond to (002) and (100) diffraction peaks for non-graphitized carbon, respectively [44]. By using Bragg's Equation, the interlayer spacing of hard carbons can be estimated (Equation (1)) [45]:

$$2d \sin \theta = n\lambda \quad (1)$$

where d is the spacing between the crystal planes (interlayer spacing), θ is the angle between the incident X-ray and the crystal plane, n is the order of reflection, and λ is the wavelength of X-ray (λ = 1.5406A° for Cu Kα radiation).

The (002) peak was deconvoluted into highly disordered and pseudo-graphitic components using a profile-fitting process to quantitatively evaluate the relative proportions of these two carbon domains. Such analysis provides deeper insight into the microstructural evolution of hard carbon, since disordered regions are generally associated with defect sites and nanopores that contribute to sodium adsorption, whereas pseudo-graphitic domains facilitate Na^+ intercalation between graphene layers (Figures S6–S9) [46]. Here, "pseudo-graphitic" denotes the fitted (002) component assigned to relatively ordered, graphite-like stacking within the adopted two-component model, rather than a separately identified crystalline phase. This label does not establish turbostratic stacking, and the fitted component area does not directly quantify active-site density or electronic transport. As shown in

Table S2, nitrogen doping markedly increases the fraction of the highly disordered component of the fitted (002) peak from 24.17% in HC to 66.39% in NHC-700, accompanied by a decrease in the pseudo-graphitic fraction to 33.61%. Further heating gradually re-establishes graphitic order, with the pseudo-graphitic area rebounding to 39.70% at 800 °C and 55.16% at 900 °C. Despite this partial restoration, the inter-layer spacing d002 of the pseudo-graphitic phase keeps widening, expanding from 0.3609 nm in HC to 0.3802 nm in NHC-900. The enlarged apparent interlayer spacings (Figure 2d) are consistent with nitrogen-associated distortion and changes in carbon-layer stacking [32,33]. However, the persistence of larger spacings as the total nitrogen content decreases indicates that nitrogen content alone cannot account for this trend; structural evolution during thermal treatment must also be considered. Therefore, the balance between disordered carbon and pseudo-graphitic domains plays an important role in determining the sodium storage behavior of hard carbon materials.

Within the adopted XRD fitting model, NHC-900 exhibits the largest apparent interlayer spacings for both the highly disordered component (0.4133 nm) and the pseudo-graphitic component (0.3802 nm). However, it does not deliver the highest reversible capacity among the investigated samples, indicating that interlayer spacing alone is insufficient to explain their electrochemical performance. Changing the treatment temperature also alters the nitrogen content and configuration, as well as the Raman spectral characteristics, so the effect of interlayer spacing cannot be isolated in this sample series. Accordingly, the results do not establish an optimal interlayer spacing or a monotonic relationship between increasing spacing and improved performance.

Taken together, the Raman and XRD results indicate structural changes associated with the modification treatment. NHC-800 exhibits the highest I_D/I_G ratio, whereas its D2 contribution is lower than that of NHC-700 and higher than that of HC. The XRD analysis gives a pseudo-graphitic interlayer spacing of 0.3708 nm for NHC-800, compared with 0.3609 nm for HC. Within the adopted two-component fitting model, the components assigned to highly disordered and pseudo-graphitic regions account for 60.30% and 39.70% of the fitted (002) peak area of NHC-800, respectively. These relative peak areas serve as model-dependent structural descriptors rather than direct measurements of the fractions of the two structural regions. The present results do not establish an optimal ratio between these components.

3.2. Surface Chemistry and Defect Engineering

X-ray photoelectron spectroscopy (XPS) was used to probe the surface composition and bonding configurations of the nitrogen-doped hard carbons (NHCs). In the survey spectra (Figure 2e), the C 1s, N 1s, and O 1s envelopes are centered at 285.00, 399.07, and 532.92 eV, respectively, confirming the coexistence of the three elements in each NHC sample [47] and there is no N 1s peak observed in pure hard carbon. Quantitative fitting gives total N contents of 4.56 at. % (NHC-700), 2.78 at. % (NHC-800), and 2.41 at. % (NHC-900); the corresponding O levels decrease from 9.49 to 7.46 at. % as the pyrolysis temperature rises. This monotonic decrease is typical of high-temperature carbonization, in which volatile N- and O-containing groups are progressively expelled, leaving a more ordered sp^2 lattice. High-resolution N 1s spectra (Figure 2f–h) can be deconvoluted into three components located at 398.43 eV (pyridinic-N), 399.29 eV (pyrrolic-N), and 400.21 eV (graphitic-N) [48]. The relative fraction of each nitrogen species was calculated by normalizing its background-subtracted N 1s peak area to the total area of the three fitted components, as summarized in Table S3 and Figure 2i. Pyridinic-N introduces localized electronic states near the Fermi level, which increase the electron density around the defect sites and strengthen Na^+ adsorption through ionic–covalent interactions, thereby expanding

the charge-storage stage [49]. Pyrrolic-N bends adjacent graphene sheets and expands interlayer spacing, thereby lowering the diffusion barrier for Na^+ intercalation and facilitating fast sodium kinetics [50]. Graphitic-N is beneficial for electronic conductivity, lacks Lewis-basic lone pairs, and therefore contributes minimally to sodium binding. Excessive graphitic-N can even reduce wettability and suppress electrolyte penetration [51,52]. From 700 °C to 800 °C, the proportion of pyridinic-N increases significantly, while the fractions of pyrrolic-N and graphitic-N decrease, indicating a thermally driven rearrangement of nitrogen configurations within the carbon framework. Thermal rearrangement converts the less stable five-membered pyrrolic rings to six-membered pyridinic rings, while a small fraction of graphitic-N is cleaved. Both pyridinic and pyrrolic nitrogen reside at edge/defect sites; the total edge-N fraction climbs to a maximum of 83.9% in NHC-800. This high density of electronegative lone-pair centers increases the carbon surface's affinity for Na^+ and provides abundant adsorption sites. From 800 °C to 900 °C, further heating only marginally reduces the total N content but drives slight graphitization and reconstructs some pyrrolic N back into the basal plane. Although graphitic-N improves electrical conductivity, it offers few active sites for Na^+ adsorption and can partially passivate pores. The net result is a modest drop in edge-N to 82.8%. These results establish differences in surface nitrogen speciation, but do not isolate the sodium-storage contributions of individual nitrogen species or oxygen-containing groups. The proposed roles of these species are therefore literature-based interpretations, since surface composition and carbon structure vary concurrently across the samples.

3.3. Electrochemical Performance Comparison

Two complementary comparisons were performed: PET-derived carbons versus rGO and MWCNTs-COOH, and HC versus NHC to examine changes accompanying the modification treatment to compare sodium-storage performance across different carbon materials under common testing conditions. These comparisons do not isolate the individual effects of nitrogen doping, additional thermal treatment, or carbon dimensionality.

The electrochemical results should also be considered in the context of the electrolyte used in this study: 1 M $NaClO_4$ in EC:DMC (1:1, v/v) without fluoroethylene carbonate (FEC). The initial irreversible capacity and subsequent cycling behavior were therefore measured under FEC-free conditions. Although the same electrolyte was used for all carbon electrodes, this does not imply that identical SEI layers formed on their different surfaces. No comparison with an FEC-containing electrolyte was performed, so the specific influence of FEC on SEI formation, initial coulombic efficiency, and cycling stability cannot be determined from the present results. Accordingly, the performance comparisons reported here are specific to the electrolyte conditions investigated.

The electrochemical performance of rGO, MWCNTs-COOH, and pristine HC was first examined to compare representative carbon architectures. Subsequently, HC and nitrogen-doped hard carbons (NHCs) were compared to evaluate the impact of nitrogen doping on electrochemical behavior. Figure 3a shows the first galvanostatic charge–discharge (GCD) curves of HC, rGO, and MWCNTs-COOH electrodes at 20 mA g^{-1}. A noticeable irreversible capacity is observed during the first cycle, mainly due to SEI formation and electrolyte decomposition. The initial coulombic efficiencies (ICEs) of HC, rGO, and MWCNTs-COOH are 81.32%, 60.21%, and 67.97%, respectively (Table S4). Figure 3b presents cycling performance curves obtained at a current density of 20 mA g^{-1}. The initial specific charge capacities for rGO, MWCNTs-COOH and HC are 79.3, 85.3 and 103.6 mAh g-1, respectively. The difference appears in the subsequent cycles. After 220 cycles, HC maintains a high reversible capacity of 80.9 mA h g^{-1}, shows higher capacity retention (78.09%) than rGO (61.29%). The oxidized MWCNTs-COOH loses activity completely after 150 cycles. HC's

outstanding performance can be attributed to its turbostratic stacking of graphitic layers; the expanded interlayer spacing accommodates Na^+ reversibly while resisting mechanical stress. For MWCNTs-COOH, the large number of edge-carboxyl groups could catalyze side reactions. The rate capability of the three samples is further investigated in Figure 3c. At low current densities (10 mA g^{-1} and 15 mA g^{-1}), there is no obvious difference in specific capacity between HC and MWCNTs-COOH. However, during high-rate testing (200 mA g^{-1}), HC still delivers 53 mAh g^{-1}, whereas rGO and MWCNTs fall to 41.5 and 30.5 mAh g^{-1}, respectively. This means that, for practical use as Na-ion anodes, HC is a better choice than rGO and MWCNTs-COOH.

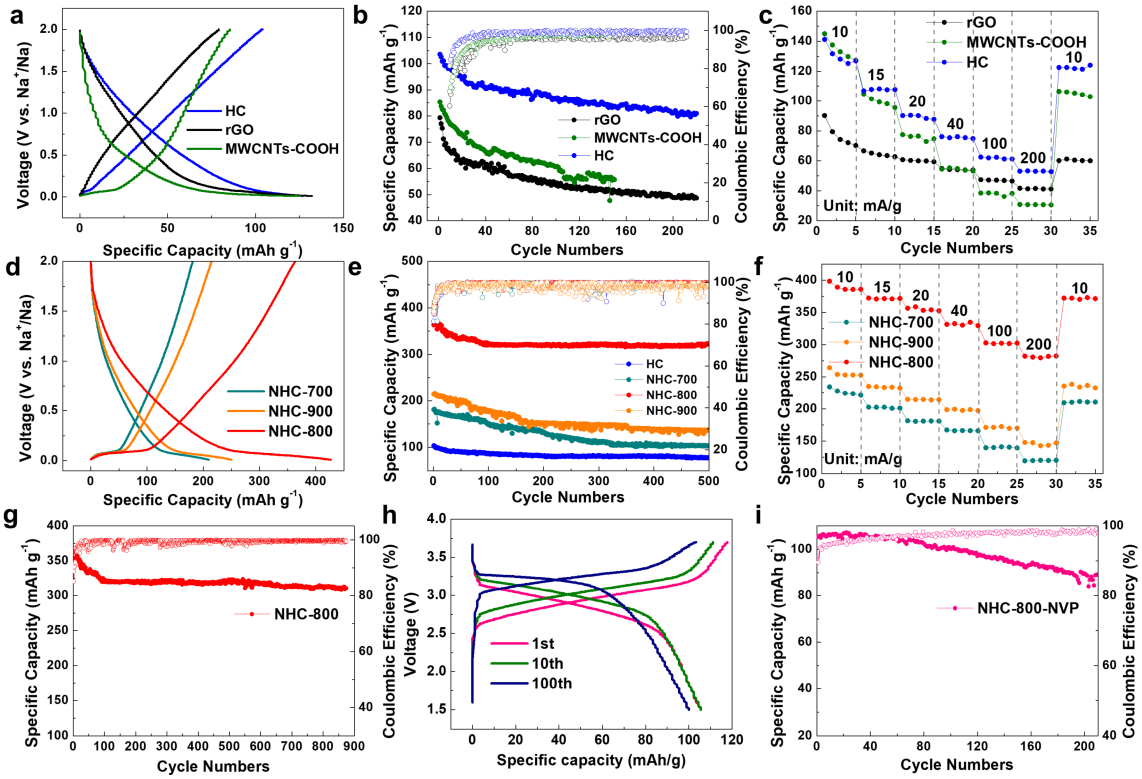


Figure 3. (**a**) The initial galvanostatic charge–discharge curves of rGO, MWCNTs-COOH and HC; (**b**) cycling performance of rGO, MWCNTs-COOH and HC under 20 mA g^{-1}; (**c**) rate performance of rGO, MWCNTs-COOH and HC from 10 mA g^{-1} to 200 mA g^{-1}; (**d**) the initial galvanostatic charge–discharge curves of NHCs; (**e**) cycling performance of HC and NHCs under 20 mA g^{-1}; (**f**) rate performance of NHCs from 10 mA g^{-1} to 200 mA g^{-1}; (**g**) long cycling performance of NHC-800 under 20 mA g^{-1}; (**h**) the initial, 10th and 100th galvanostatic charge–discharge curves of the full-cell NHC-800//NVP; (**i**) cycling performance of the full-cell NHC-800//NVP under 20 mA g^{-1}.

Secondly, we studied the performance of the N-doped HC prepared at different temperatures. The first charge–discharge curves for NHC-700, NHC-800, and NHC-900 samples are presented in Figure 3d. The ICEs of NHC-700, NHC-800, and NHC-900 are 86.27%, 85.15%, and 85.98%, respectively (Table S4), compared with 81.32% for undoped HC. Notably, HC and NHC-800 retain high BET specific surface areas of 560.25 and 478.34 m^2 g^{-1}, respectively. The higher ICE of NHC-800 should therefore not be attributed solely to its lower BET surface area. Although all NHC samples exhibit higher ICEs than HC, NHC-800 does not have the highest ICE in NHC series. Its ICE of 85.15% still indicates appreciable first-cycle irreversible capacity, which cannot be assigned exclusively to SEI formation. In a full cell with a finite sodium inventory, irreversible sodium consumption reduces the sodium available for subsequent cycling and can limit the achievable energy density. Further improvements in ICE, for example through electrolyte optimization or

controlled presodiation, would therefore be needed to strengthen practical applicability. All the curves have a sloping region, followed by a steep low-voltage plateau (<0.1 V). The nitrogen configuration plays an important role in NHCs performance. NHC-800 exhibits the highest combined relative fraction of pyridinic and pyrrolic N, accounting for 83.9% of the total nitrogen content and these N sites can introduce surface defects that strengthen Na adsorption. At higher temperatures (900 °C), some of these sites convert to graphitic N, reducing active-site density. At 700 °C, excessive surface heteroatoms and oxygenated groups intensify SEI formation. Meanwhile, N_2 adsorption–desorption test results show NHC-800 has a lower specific surface area than HC, indicating less fresh carbon is exposed to the electrolyte. Furthermore, XRD calculations indicate that the interlayer spacing of the pseudo-graphitic area in NHC-800 is 0.3708 nm, which is suitable for Na^+ intercalation [10]. These three factors contribute to the satisfactory performance of NHC-800. Cycling performance for NHCs and HC is displayed in Figure 3e, all NHCs surpass pristine HC, indicative of successful electronic/ionic tuning by nitrogen. NHC-800 reaches 322.3 mAh g^{-1} after 500 cycles, NHC-900 and NHC-700 settle at 136.4 and 103.1 mAh g^{-1}, still higher than HC (77.8 mAh g^{-1}), confirming that nitrogen doping contributes to sodium storage. In terms of rate capability, when the current density steps from 10 to 200 mA g^{-1}, the specific capacities of NHCs gradually decline (Figure 3f). Upon returning to 10 mA g^{-1}, the capacities nearly fully recover, indicating the mechanical integrity and elastic deformability of the disordered carbon matrix.

For long cycling performance of optimized NHC-800 (Figure 3g), it exhibits a reversible capacity of 310.7 mAh g^{-1} with 85.6% capacity retention over 874 cycles. The long-term cycling stability of NHC-800 may be associated with its nitrogen configurations and carbon microstructure, as characterized by XPS and XRD, although the individual contributions of these features cannot be isolated from the present results. Figure 3h shows the charge–discharge profiles of the NHC-800//NVP full cell at the 1st, 10th, and 100th cycles. Distinct voltage plateaus corresponding to the Na^+ insertion/extraction reaction of the NVP cathode are clearly observed. The charge–discharge curves largely overlap during cycling, indicating good reversibility and stable electrochemical behavior. The full cell delivered an initial discharge capacity of 105.6 mAh g^{-1}, normalized to the NHC-800 anode active-material mass, with an average discharge voltage of 2.74 V. Integration of the first-cycle discharge voltage–capacity curve yielded a specific energy of 86.3 Wh kg^{-1} based on the combined active-material mass of the NVP cathode (3.3 mg) and NHC-800 anode (1.4 mg). This value excludes the masses of the current collectors, binder, conductive additive, separator, electrolyte, and cell casing. As shown in Figure 3i, the NHC-800//NVP full cell exhibits excellent cycling stability with a capacity retention of 84.5% after over 200 cycles. A comparison of the preparation procedures, structural characteristics, and electrochemical performance of the present materials with selected literature-reported hard-carbon anodes is provided in Table S5.

A broader comparison can be drawn with the $MnCo_2O_4$/PANI nanohybrid reported by Zaman et al. [53], which combines a metal oxide with a conducting polymer for supercapacitor applications. Whereas that approach integrates distinct material components, the present study modifies the chemistry and microstructure of a carbon framework through nitrogen doping and thermal treatment. Both approaches motivate consideration of electrochemically accessible sites together with charge-transport pathways when interpreting electrode performance. However, the different electrode chemistries, electrolytes, and storage processes preclude direct quantitative performance comparisons.

3.4. Comparative Sodium-Storage Kinetics and Mechanisms of HC, NHC, MWCNTs-COOH and rGO

Cyclic voltammetry (CV) tests were conducted in the voltage range from 0 to 2.5 V at a scan rate of 0.1 mV s^{-1} to probe the electrochemical behavior of rGO, MWCNTs-COOH, HC, and NHC-800. The initial three-cycle CV curves of these carbon electrodes are presented in Figures S10–S13. Several common findings emerge; however, the subtleties among rGO, MWCNTs-COOH, HC, and NHC-800 offer valuable clues to their sodium-storage mechanisms and kinetics. During the initial cycle, all the electrodes exhibit an irreversible reduction peak centered at 0.42 V. The appearance of these peaks is widely attributed to the formation of the solid electrolyte interphase (SEI) layer, where the electrolyte decomposes on the electrode surface, and some irreversible chemical reactions occur. There is a broad, not readily apparent reduction peak at around 0.86 V in the rGO, HC, and NHC-800 samples, which may be due to the reduction of residual surface functional groups. Stable interphase is established after the first sodiation step, as evidenced by the disappearance of these irreversible peaks in subsequent cycles. At nearly 0.01 V, a sharp reduction peak appears, indicating sodium storage across all curves. For MWCNTs-COOH, HC, and NHC-800, oxidation peaks are observed at approximately 0.11, 0.09, and 0.13 V, respectively, indicating sodium release. These redox couples represent the Na^+ insertion/extraction process in hard-carbon-type anodes [54]. However, no obvious oxidation peak emerges in the first three scans for rGO. The absence of a clear anodic peak in rGO suggests sluggish desodiation, explaining its modest reversible capacity. It is worth noting that the desodiation peaks of MWCNTs-COOH, HC, and especially NHC-800 sharpen and intensify from the 2nd to the 3rd cycle, signaling lower charge-transfer resistance and electrode activation [55]. The redox peak current reflects the extent of the Faradaic reaction in the voltage range where redox peaks appear. Generally speaking, the Faradaic reaction is a chemical reaction with electron transfer. In our case, this reaction represents the desodiation/sodiation process. When the peak current increases, there are more sodium ions involved in this process [20].

The sodium storage kinetics of various carbon electrodes were further elucidated by CV scanning at scan rates from 0.1 to 1 mV s^{-1}. It is commonly known that the electrochemical reaction of sodium with carbon electrodes contains two processes: a diffusion-controlled process and a capacitive-controlled process. The way the current response is generated during electrochemical reactions is different. For a diffusion-controlled process, the current is limited by the speed at which sodium ions diffuse from the electrolyte into the bulk of the electrode material [56]. This slow process depends on ion mobility and material structure. In terms of a capacitive-controlled process, the current comes from charge storage at or near the surface and does not require ion diffusion into the bulk [57]. In order to distinguish sodium storage kinetics, the following equation is employed to calculate the b value [41]:

$$i = av^b \tag{2}$$

This equation relates the peak current i to the scan rate v, where a is a constant and b is estimated by linear fitting. When b approaches 0.5, the entire reaction is controlled by diffusion, while b equals 1.0 means capacitive behavior, such as sodium ion adsorption on defects, edges, and functional groups.

Capacitive contribution of current is evaluated through deconvolution of current profiles using the equation as follows [58]:

$$i(V) = k_1 v + k_2 v^{\frac{1}{2}} \tag{3}$$

where k_1v denotes the capacitive-controlled contribution in the exact current, and $k_2v^{1/2}$ reflects the diffusion-controlled contribution.

The peak-current b-value analysis describes the scan-rate dependence of the selected redox peaks, whereas the Dunn analysis estimates capacitive and diffusion-controlled current contributions at each potential using the relationship $i(V) = k_1(V)v + k_2(V)v^{1/2}$. Accordingly, the fitted b-values should not be interpreted as capacitive fractions or directly equated with contributions integrated over the analyzed potential range. As both analyses are derived from the same CV dataset, they provide complementary kinetic descriptions rather than independent validation of a specific sodium-storage mechanism.

The fitted b-values and corresponding coefficients of determination (R^2) for both selected peaks of each electrode material are summarized in Table S6. As shown in Figures S14, S15 and 4a, all three electrodes exhibit a pair of well-defined cathodic/anodic peaks in the CV curves, indicating a typical pattern of reversible Na^+ uptake/release. Meanwhile, as scan rates increase, enhanced potential polarization is observed across all samples. rGO and MWCNTs-COOH exhibit predominantly diffusion-controlled sodium-storage kinetics, as indicated by their b values close to 0.5–0.6 (Figures S16 and S17). For rGO, the b values of Peaks 1 and 2 are 0.56 and 0.57, respectively, suggesting that Na^+ storage mainly involves diffusion into accessible intersheet regions, accompanied by adsorption at sheet edges and residual defects. For MWCNTs-COOH, the corresponding b values are 0.53 and 0.66. The cathodic process is therefore primarily diffusion-controlled, whereas the relatively higher anodic b value indicates a greater surface-controlled contribution during Na extraction. Nevertheless, these b values describe the overall rate dependence of the peak current and do not reveal the pronounced sodiation–desodiation asymmetry identified by GITT, as discussed below. The situation is different for HC; b values for peaks 1 and 2 are 0.74 and 0.62, respectively, indicating hybrid behavior and fast surface kinetics (Figure S18). Figure 4d–f corroborate the b-value diagnosis. At the lowest scan rate (0.1 mV s^{-1}) diffusion governs in all cases because ions have ample time to penetrate the bulk.

When the scan rate rises to 1 mV s^{-1}, the capacitive contribution of rGO climbs from 28% to 55%, while that of MWCNTs-COOH increases from 22% to 47%; these results are consistent with the b values and confirm that bulk or confined diffusion remains dominant under near-equilibrium conditions. Capacitive contribution of HC soars to 73% at 1 mV s^{-1}; even at 0.1 mV s^{-1}, the capacitive contribution remains 47%, confirming the hybrid nature of hard carbon. Widely distributed nanopores and an amorphous lattice in HC provide short solid-state paths and abundant adsorption sites, explaining its high pseudocapacitance and good high-rate capacity.

Compared with HC, all the nitrogen-doped samples exhibit the familiar pair of Na^+ insertion/extraction peaks, but the anodic current is visibly larger, which means intensive Faradaic reactions happen (Figures S19, S20 and 4b). The expanded interlayer spacing of NHCs lowers the Na^+ intercalation barrier, and the increased number of active sites in NHCs promotes adsorption. Nitrogen doping temperature affects sodium storage behavior to some extent; linear-fitting results of peak 1 and peak 2 in NHC-700 are 0.70 and 0.71, respectively (Figure S21). This clear hybrid behavior is caused by high nitrogen content (4.6 at. %). b values of peak 1 and peak 2 in NHC-800 are slightly higher than those in the samples in 700 °C and 900 °C, which are about 0.8 and 0.7, respectively (Figure 4c). The capacitive-controlled process is more active in NHC-800. When the temperature keeps going up to 900 °C (Figure S22), the b value decreases a little, indicating that high temperature removes some active sites (lower N and O contents). Figure 4g–i convert each CV curve into quantitative fractions. At 0.1 mV s^{-1}, NHC-800 already dedicates 57% of its charge to fast surface mechanisms. When the scan rate goes up to 0.6–0.8 mV s^{-1}, NHC-800 preserves the highest capacitive contribution. At 1 mV s^{-1}, NHC-800 has the highest capacitive contribution among the three samples. These figures echo the b-value trend and confirm that NHC-800 delivers the best hybrid behavior.

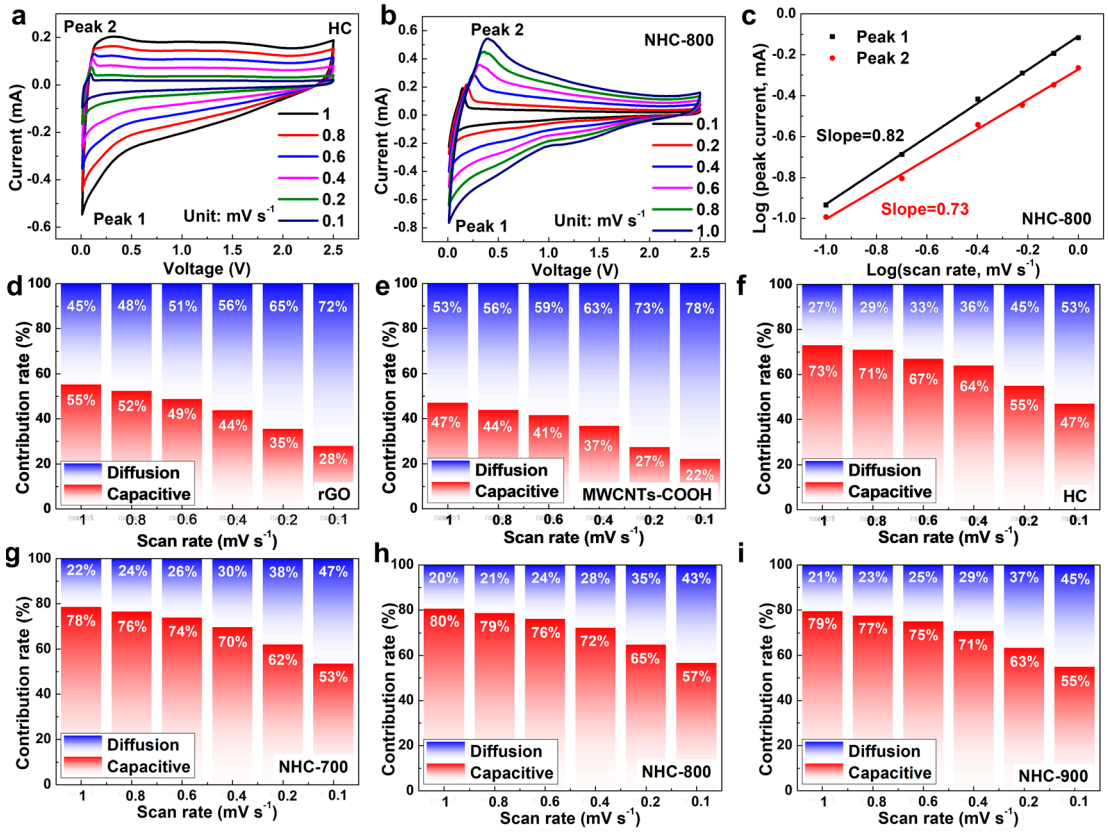


Figure 4. (**a**) CV curves of HC at various scan rates from 0.1 to 1 mV s^{-1}; (**b**) CV curves of NHC-800 at various scan rates from 0.1 to 1 mV s^{-1}; (**c**) the correlations of scan rate (v) and peak current (i) of NHC-800; (**d**) capacitive contributions of rGO at various scanning rates; (**e**) capacitive contributions of MWCNTs-COOH at various scanning rates; (**f**) capacitive contributions of HC at various scanning rates; (**g**) capacitive contributions of NHC-700 at various scanning rates; (**h**) capacitive contributions of NHC-800 at various scanning rates; (**i**) capacitive contributions of NHC-900 at various scanning rates.

The diffusion coefficient of Na^+ is a crucial parameter to evaluate the ion diffusion and sodium storage mechanism. The galvanostatic intermittent titration (GITT) technique is a convenient tool to measure the diffusion coefficient during the charge–discharge process. In the theory of GITT, diffusion in the solid electrode is simply assumed to be one-dimensional, and several effects are neglected, such as double-layer charging and Ohmic potential drop [59]. A pulse current is first applied to the system during time τ as a transient process. The entire system then experiences relaxation (no current applied) for equilibrium, where voltage is monitored. For hard carbon electrodes, a 20 mA g^{-1} constant current is employed for 30 min pulse time, with a rest interval of 2 h. Calculating from Fick's second law of diffusion, the following equation provides a solution for the diffusion coefficient of Na^+ [60,61]:

$$D_{Na,app} = \frac{4}{\pi\tau}\left(\frac{m_a V_m}{M_a S}\right)^2\left(\frac{\Delta E_S}{\Delta E_\tau}\right)^2 \quad (4)$$

Here, $D_{Na,app}$ is the apparent Na^+ diffusion coefficient (cm^2 s^{-1}), τ is the current-pulse duration (1800 s), ma is the active-material mass (g), Ma is its molar mass (g mol^{-1}), Vm is its molar volume (cm^3 mol^{-1}), and S is the electrode–electrolyte contact area adopted in the calculation (cm^2). ΔEs is the difference between the relaxed potentials before and after the current pulse, whereas ΔEτ is the potential change during the pulse after excluding the instantaneous IR drop. This simplified expression assumes short-time diffusion and an approximately linear dependence of potential on the square root of time over the analyzed

interval. The resulting values are treated as apparent diffusion coefficients within these model assumptions.

The Na^+ diffusion coefficients of rGO, MWCNTs-COOH, HC, and NHC-800 during sodiation and desodiation are compared in Figure 5a. For rGO, the diffusion coefficient remains relatively stable at approximately 10–12.1 cm^2 s^{-1} during sodiation, suggesting a broadly distributed diffusion-controlled process involving Na^+ adsorption at sheet edges and residual defects, followed by migration into accessible intersheet spaces. During desodiation, rGO maintains comparatively high diffusion coefficients of approximately 10–12.4 to 10–12.0 cm^2 s^{-1}. The origin of the limited capacity retention of rGO remains unresolved in the present study, as no post-cycling structural characterization was performed to establish the underlying structural changes.

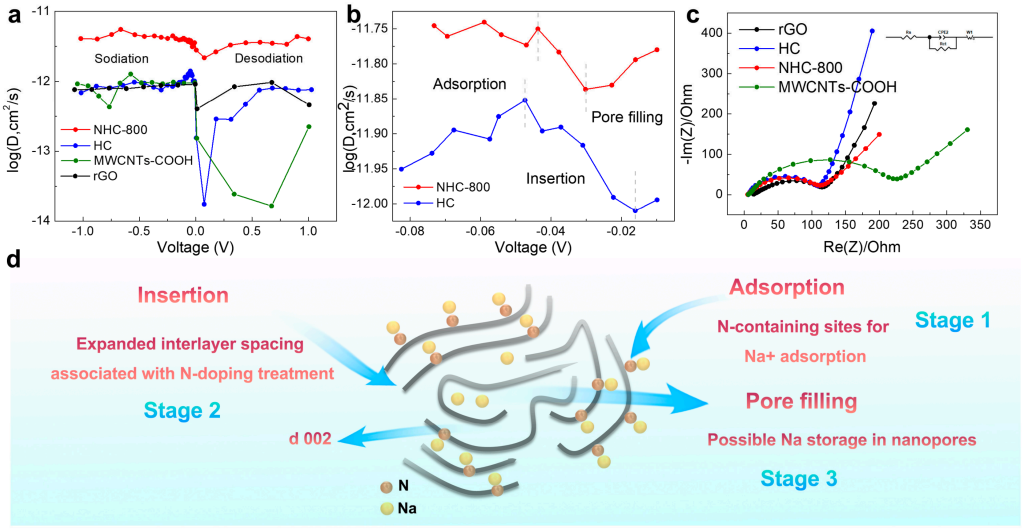


Figure 5. (**a**) Na^+ diffusion coefficients of rGO, MWCNTs-COOH, HC, and NHC-800 during sodiation and desodiation. (**b**) Diffusion coefficients of sodium ions during the sodiation process of HC and NHC-800 (GITT measurements were performed on one cell per material ($n = 1$). Replicate-based error bars are not available.). (**c**) EIS of rGO, MWCNTs-COOH, HC and NHC-800. (**d**) Schematic illustration of the proposed role of nitrogen doping in sodium storage, showing N-containing sites for Na^+ adsorption, expanded interlayer spacing associated with the nitrogen-doping treatment, and possible sodium storage in nanopores. The schematic is based on literature-reported interpretations [32,33,62] and does not establish a definitive sequence of storage processes.

MWCNTs-COOH exhibits similarly high diffusion coefficients during most of the sodiation process, although a localized minimum is observed, which may reflect the transition from adsorption at oxygenated surface defects to the occupation of more confined interwall, interbundle, or internal sites. A markedly different behavior occurs during desodiation, where the diffusion coefficient decreases to approximately 10–13.6 to 10–13.8 cm^2 s^{-1} over the intermediate-potential region. This pronounced kinetic asymmetry indicates that Na^+ can enter the oxidized nanotube structure relatively readily but experiences substantial resistance during extraction. Strong interactions with oxygen-containing defects, geometrically confined storage sites, and an unstable interphase may collectively contribute to this behavior. In contrast to the broadly distributed storage behavior of rGO and the strongly asymmetric behavior of MWCNTs-COOH, the GITT profiles of HC and NHC-800 are tentatively interpreted within the adsorption–intercalation–pore-filling framework proposed in previous studies [62]. Figure 5d schematically highlights N-containing sites for Na^+ adsorption and enlarged interlayer spacing associated with the nitrogen-doping treatment that may facilitate Na^+ insertion [32,33], alongside possible sodium storage in nanopores [62].

This literature-based interpretation does not establish the occurrence or sequence of these processes. The individual effects of nitrogen incorporation and the accompanying thermal treatment cannot be isolated here. At relatively high potentials, Na^+ is predominantly adsorbed at surface defects and active sites. The subsequent decrease in the diffusion coefficient corresponds to Na^+ insertion into pseudo-graphitic layers, whereas its recovery at the lowest potentials is associated with the occupation of closed or semi-closed nanopores. In particular, the low-potential plateau and the accompanying variation in the apparent diffusion coefficient are not unique signatures of nanopore filling and do not exclude interlayer insertion or other sodium-storage processes. Nanopore filling is therefore considered a possible contribution within the literature-reported framework [62], rather than a mechanism independently established by the present measurements. During desodiation, HC exhibits a pronounced minimum followed by a recovery in the GITT-derived apparent diffusion coefficient. This feature reflects changes in the relative relaxed and pulse-induced potential responses during sodium extraction, but the present data do not uniquely establish its mechanistic origin.

The GITT-derived apparent diffusion coefficients of HC and NHC-800 are of a similar order of magnitude. Each material was measured using one cell ($n = 1$), and cell-to-cell variability was therefore not assessed. The small differences between the two profiles cannot be established as statistically significant and are not taken as evidence of intrinsically faster Na+ diffusion in NHC-800.

Overall, the four carbon materials exhibit different GITT-derived apparent diffusion-coefficient profiles. For rGO, the apparent Na^+ diffusion coefficient remains relatively stable during sodiation and varies within a comparatively narrow range during desodiation; MWCNTs-COOH permits comparatively facile sodiation but suffers from severely hindered desodiation from oxygenated and structurally confined sites; HC exhibits reversible adsorption, interlayer insertion, and nanopore filling; and NHC-800 optimizes all three contributions through the synergistic regulation of N-containing defects, interlayer spacing, and pore structure.

The macroscopic GITT pulse response is shown in Figures S23–S26; ΔEs and ΔEτ can be obtained from this curve. Electrochemical impedance spectroscopy (EIS) results for rGO, MWCNTs-COOH, HC and NHC-800 are displayed in Figure 5c. In the high-frequency region of spectra, a semicircle exists in all samples, which is caused by the charge transfer resistance (Rct), while the ion diffusion impedance (Zw) inside electrodes appears as a straight line in the low-frequency region. The fitted charge-transfer resistances of NHC-800 and HC are 97.32 and 106.45 Ω, respectively (Table S7). Although the fitted value for NHC-800 is numerically lower, EIS was measured on one cell per material ($n = 1$), and the reproducibility of this difference has not been established. The two values are therefore regarded as comparable in magnitude rather than evidence of a definitive enhancement in charge-transfer kinetics. MWCNTs-COOH exhibits the highest fitted Rct of 219.26 Ω under the investigated conditions. This may reflect differences in surface chemistry, interphase properties, and electrochemically accessible area, rather than intrinsically poor electronic conductivity of the nanotubes. However, without an untreated-MWCNT control or direct interphase characterization, the dominant origin of this higher resistance remains unresolved. The EIS result alone does not establish the cause of the observed desodiation behavior or capacity decay.

4. Conclusions

This study evaluated PET-derived nitrogen-doped hard carbon as a sodium-ion battery anode and compared its electrochemical behavior with undoped HC, rGO, and MWCNTs-COOH. Among the investigated samples, NHC-800 delivered a reversible capacity of

310.7 mAh g^{-1} after 874 cycles at 20 mA g^{-1}, corresponding to a capacity retention of 85.6%. Its initial coulombic efficiency was 85.15%, compared with 81.32% for HC. The NHC-800//NVP full cell, assembled using a presodiated NHC-800 anode, retained 84.5% of its reference capacity over approximately 200 cycles, providing a preliminary demonstration of full-cell operation.

A key contribution of this work is the combined evaluation of PET-derived HC and NHC alongside rGO and MWCNTs-COOH under common electrochemical testing conditions. This comparison places the performance of the waste-plastic-derived carbons within a broader set of carbon electrode materials. Relative to HC, NHC-800 exhibits a lower BET specific surface area (478.34 versus 560.25 m^2 g^{-1}), a higher I_D/I_G ratio (1.20 versus 1.06), and larger apparent interlayer spacings obtained from XRD fitting. Together with the XPS characterization of nitrogen configurations, these results document the structural and compositional changes accompanying the modification treatment. The electrochemical results identify NHC-800 as the best-performing sample in the investigated series in terms of long-term reversible capacity, highlighting the potential of waste PET as a precursor for sodium-storage carbon materials.

Nevertheless, the individual contributions of the coupled material changes, the reproducibility of the GITT/EIS comparisons, and the practical full-cell energy performance remain to be established. Future work should prioritize replicate-cell measurements to quantify variability in the kinetic and cycling results, together with matched thermal-treatment controls to distinguish the effects of nitrogen incorporation from those of additional heat treatment. Potential-resolved structural and chemical characterization should be used to test the proposed sodium-storage processes. Full-cell evaluation should include documented electrode loadings and electrolyte volumes, energy calculations with explicit mass-normalization bases, and testing at higher current densities and extended cycle numbers. These steps would clarify the origin of the observed performance and enable a more rigorous assessment of practical applicability.

Supplementary Materials: The following supporting information can be downloaded at: https://www.mdpi.com/article/10.3390/batteries12110491/s1, Figure S1: HRTEM and FFT images of NHC-800; Figure S2: Raman fitting curves of HC; Figure S3: Raman fitting curves of NHC-700; Figure S4: Raman fitting curves of NHC-800; Figure S5: Raman fitting curves of NHC-900; Figure S6: XRD fitting curves of HC; Figure S7: XRD fitting curves of NHC-700; Figure S8: XRD fitting curves of NHC-800; Figure S9: XRD fitting curves of NHC-900; Figure S10: Cyclic voltammograms of rGO at 0.1 mV s^{-1}; Figure S11: Cyclic voltammograms of MWCNTs-COOH at 0.1 mV s^{-1}; Figure S12: Cyclic voltammograms of HC at 0.1 mV s^{-1}; Figure S13: Cyclic voltammograms of NHC-800 at 0.1 mV s^{-1}; Figure S14: CV curves of rGO at various scan rates from 0.1 to 1 mV s^{-1}; Figure S15: CV curves of MWCNTs-COOH at various scan rates from 0.1 to 1 mV s^{-1}; Figure S16: The correlations of current scan rate (v) and peak current (i) of rGO; Figure S17: The correlations of current scan rate (v) and peak current (i) of MWCNTs-COOH; Figure S18: The correlations of current scan rate (v) and peak current (i) of HC; Figure S19: CV curves of NHC-700 at various scan rates from 0.1 to 1 mV s^{-1}; Figure S20: CV curves of NHC-900 at various scan rates from 0.1 to 1 mV s^{-1}; Figure S21: The correlations of current scan rate (v) and peak current (i) of NHC-700; Figure S22: The correlations of current scan rate (v) and peak current (i) of NHC-900; Figure S23: The macroscopic GITT pulse response of NHC-800; Figure S24: The macroscopic GITT pulse response of HC; Figure S25: The macroscopic GITT pulse response of rGO; Figure S26: The macroscopic GITT pulse response of MWCNTs-COOH; Table S1: Physical parameters of the hard carbon samples from Raman spectra; Table S2: Physical parameters of the hard carbon samples from XRD patterns; Table S3: Relative percentage of different nitrogen species for NHCs; Table S4: Initial coulombic efficiency (ICE) of electrode materials; Table S5: Comparison of preparation procedures, structural characteristics, and sodium-storage performance of the present materials and selected literature-reported hard-carbon anodes; Table S6: Fitted b-values and corresponding coefficients of determination (R^2) for the two selected CV peaks of the investigated carbon electrodes; Table S7: EIS fitting results of electrode materials; Supplementary Methods: Calculation of the N/P capacity ratio.

Author Contributions: Conceptualization, Q.L.; methodology, Q.L. and A.Y.; software, Q.L.; validation, Q.L.; formal analysis, Q.L.; investigation, Q.L., W.Z. and S.H.; resources, Q.L., A.G.M., T.H.M. and A.Y.; data curation, Q.L.; writing—original draft preparation, Q.L.; writing—review and editing, Q.L., Y.H. and A.Y.; visualization, Q.L.; supervision, A.Y.; project administration, A.Y.; funding acquisition, A.Y. All authors have read and agreed to the published version of the manuscript.

Funding: This research was funded by the Natural Sciences and Engineering Research Council of Canada (NSERC).

Data Availability Statement: The data presented in this study are available in the article and its Supplementary Materials. Additional data supporting the findings of this study are available from the corresponding author upon reasonable request.

Conflicts of Interest: The authors declare no conflict of interest.

References

1. Nayak, P.K.; Yang, L.; Brehm, W.; Adelhelm, P. From Lithium-Ion to Sodium-Ion Batteries: Advantages, Challenges, and Surprises. *Angew. Chem. Int. Ed.* **2018**, *57*, 102–120. [CrossRef] [PubMed]
2. Hwang, J.-Y.; Myung, S.-T.; Sun, Y.-K. Sodium-ion batteries: Present and future. *Chem. Soc. Rev.* **2017**, *46*, 3529–3614. [CrossRef] [PubMed]
3. Schäfer, D.; Hankins, K.; Allion, M.; Krewer, U.; Karcher, F.; Derr, L.; Schuster, R.; Maibach, J.; Mück, S.; Kramer, D.; et al. Multiscale Investigation of Sodium-Ion Battery Anodes: Analytical Techniques and Applications. *Adv. Energy Mater.* **2024**, *14*, 2302830. [CrossRef]
4. Perveen, T.; Siddiq, M.; Shahzad, N.; Ihsan, R.; Ahmad, A.; Shahzad, M.I. Prospects in anode materials for sodium ion batteries-A review. *Renew. Sustain. Energy Rev.* **2020**, *119*, 109549. [CrossRef]
5. Liu, Y.; Merinov, B.V.; Goddard, W.A., 3rd. Origin of low sodium capacity in graphite and generally weak substrate binding of Na and Mg among alkali and alkaline earth metals. *Proc. Natl. Acad. Sci. USA* **2016**, *113*, 3735–3739. [CrossRef] [PubMed]
6. Luo, X.-F.; Yang, C.-H.; Peng, Y.-Y.; Pu, N.-W.; Ger, M.-D.; Hsieh, C.-T.; Chang, J.-K. Graphene nanosheets, carbon nanotubes, graphite, and activated carbon as anode materials for sodium-ion batteries. *J. Mater. Chem. A* **2015**, *3*, 10320–10326. [CrossRef]
7. Xie, L.; Tang, C.; Bi, Z.; Song, M.; Fan, Y.; Yan, C.; Li, X.; Su, F.; Zhang, Q.; Chen, C. Hard Carbon Anodes for Next-Generation Li-Ion Batteries: Review and Perspective. *Adv. Energy Mater.* **2021**, *11*, 2101650. [CrossRef]
8. Shao, W.; Shi, H.; Jian, X.; Wu, Z.-S.; Hu, F. Hard-Carbon Anodes for Sodium-Ion Batteries: Recent Status and Challenging Perspectives. *Adv. Energy Sustain. Res.* **2022**, *3*, 2200009. [CrossRef]
9. Wang, D.; Zhou, J.; Li, Z.; Li, J.; Hou, L.; Gao, F. Uniformly expanded interlayer distance to enhance the rate performance of soft carbon for lithium-ion batteries. *Ionics* **2019**, *25*, 1531–1539. [CrossRef]
10. Zhao, L.-F.; Hu, Z.; Lai, W.-H.; Tao, Y.; Peng, J.; Miao, Z.-C.; Wang, Y.-X.; Chou, S.-L.; Liu, H.-K.; Dou, S.-X. Hard Carbon Anodes: Fundamental Understanding and Commercial Perspectives for Na-Ion Batteries beyond Li-Ion and K-Ion Counterparts. *Adv. Energy Mater.* **2021**, *11*, 2002704. [CrossRef]
11. Wu, C.; Yang, Y.; Zhang, Y.; Xu, H.; He, X.; Wu, X.; Chou, S. Hard carbon for sodium-ion batteries: Progress, strategies and future perspective. *Chem. Sci.* **2024**, *15*, 6244–6268. [CrossRef] [PubMed]
12. Jia, Q.; Li, Z.; Ruan, H.; Luo, D.; Wang, J.; Ding, Z.; Chen, L. A Review of Carbon Anode Materials for Sodium-Ion Batteries: Key Materials, Sodium-Storage Mechanisms, Applications, and Large-Scale Design Principles. *Molecules* **2024**, *29*, 4331. [CrossRef] [PubMed]
13. Dai, L.; Karakas, O.; Cheng, Y.; Cobb, K.; Chen, P.; Ruan, R. A review on carbon materials production from plastic wastes. *Chem. Eng. J.* **2023**, *453*, 139725. [CrossRef]
14. Chen, Z.; Wei, W.; Ni, B.-J.; Chen, H. Plastic wastes derived carbon materials for green energy and sustainable environmental applications. *Environ. Funct. Mater.* **2022**, *1*, 34–48. [CrossRef]
15. Li, S.; Cho, M.-K.; Deng, S.; Wang, J.; Lee, K.B. Upcycling of polyethylene terephthalate waste into porous carbon as potential CO2 adsorbents through autogenic pressure carbonization. *Chem. Eng. J.* **2024**, *494*, 152931. [CrossRef]
16. Ren, S.; Xu, X.; Hu, K.; Tian, W.; Duan, X.; Yi, J.; Wang, S. Structure-oriented conversions of plastics to carbon nanomaterials. *Carbon Res.* **2022**, *1*, 15. [CrossRef]
17. Yaqoob, L.; Noor, T.; Iqbal, N. Conversion of Plastic Waste to Carbon-Based Compounds and Application in Energy Storage Devices. *ACS Omega* **2022**, *7*, 13403–13435. [CrossRef] [PubMed]
18. Wang, Y.; Jiang, M.; Wu, D.; Xiong, C. Plastic-derived carbons for high-performance battery electrodes: Upcycling, design strategies, and perspectives. *Green Chem.* **2025**, *27*, 13968–13992. [CrossRef]

19. Wang, C.; Luo, M.; Song, S.; Tang, M.; Wang, X.; Liu, H. Tuning the Mesopore Structure of Polyethylene Glycol Terephthalate (PET)-Derived Hard Carbon for High-Capacity Sodium-Ion Batteries. *Materials* **2025**, *18*, 1166. [CrossRef] [PubMed]
20. Li, N.; Li, H.; Huang, H. Synergistic Nitrogen-Doping and Defect Engineering in Hard Carbon: Unlocking Ultrahigh Rate Capability and Long-Cycling Stability for Sodium-Ion Battery Anodes. *Materials* **2025**, *18*, 2397. [CrossRef] [PubMed]
21. Ma, Z.-H.; Yang, T.; Song, Y.; Tian, X.-D.; Liu, Z.-Y.; Gong, X.-J.; Liu, Z.-J. Preparation of nitrogen doped hyper-crosslinked polymer-based hard carbon for high performance Li+/Na+ battery anode. *J. Colloid Interface Sci.* **2024**, *661*, 436–449. [CrossRef] [PubMed]
22. Song, Z.; Di, M.; Chen, S.; Bai, Y. Three-dimensional N/O co-doped hard carbon anode enabled superior stabilities for sodium-ion batteries. *Chem. Eng. J.* **2023**, *470*, 144237. [CrossRef]
23. Zhang, P.; Shu, Y.; Zhong, B.; Yang, L.; Guo, X. Optimizing sodium storage mechanisms and electrochemical performance of high Nitrogen-Doped hard carbon anode materials Derived from waste plastics for Sodium-Ion batteries. *Chem. Eng. J.* **2024**, *498*, 155231. [CrossRef]
24. Marcano, D.C.; Kosynkin, D.V.; Berlin, J.M.; Sinitskii, A.; Sun, Z.; Slesarev, A.; Alemany, L.B.; Lu, W.; Tour, J.M. Improved Synthesis of Graphene Oxide. *ACS Nano* **2010**, *4*, 4806–4814. Correction in *ACS Nano* **2018**, *12*, 2078. https://doi.org/10.1021/acsnano.8b00128. [CrossRef] [PubMed]
25. Blanchard, R.; Mekonnen, T.H. Synchronous pyrolysis and activation of poly (ethylene terephthalate) for the generation of activated carbon for dye contaminated wastewater treatment. *J. Environ. Chem. Eng.* **2022**, *10*, 108810. [CrossRef]
26. Patel, A.; Mishra, R.; Tiwari, R.K.; Tiwari, A.; Samriddhi; Singh, S.P.; Yadav, V.; Singh, R.K. Nitrogen-Doped Bioderived Mesoporous Hard Carbon as a Promising Anode for Long-Life Sodium-Ion Battery. *Energy Fuels* **2024**, *38*, 11262–11274. [CrossRef]
27. Selinger, J.; Stock, S.; Schlemmer, W.; Hobisch, M.; Kostoglou, N.; Abbas, Q.; Paris, O.; Mitterer, C.; Hummel, M.; Spirk, S. Nanoporous Carbon Electrodes Derived from Coffee Side Streams for Supercapacitors in Aqueous Electrolytes. *Nanomaterials* **2022**, *12*, 2647. [CrossRef] [PubMed]
28. Nölle, R.; Beltrop, K.; Holtstiege, F.; Kasnatscheew, J.; Placke, T.; Winter, M. A reality check and tutorial on electrochemical characterization of battery cell materials: How to choose the appropriate cell setup. *Mater. Today* **2020**, *32*, 131–146. [CrossRef]
29. Alvin, S.; Yoon, D.; Chandra, C.; Cahyadi, H.S.; Park, J.-H.; Chang, W.; Chung, K.Y.; Kim, J. Revealing sodium ion storage mechanism in hard carbon. *Carbon* **2019**, *145*, 67–81. [CrossRef]
30. Zeng, F.; Xing, L.; Zhang, W.; Xie, Z.; Liu, M.; Lin, X.; Tang, G.; Mo, C.; Li, W. Innovative discontinuous-SEI constructed in ether-based electrolyte to maximize the capacity of hard carbon anode. *J. Energy Chem.* **2023**, *79*, 459–467. [CrossRef]
31. Cordero, B.; Gómez, V.; Platero-Prats, A.E.; Revés, M.; Echeverría, J.; Cremades, E.; Barragán, F.; Alvarez, S. Covalent radii revisited. *Dalton Trans.* **2008**, *37*, 2832–2838. [CrossRef] [PubMed]
32. Feng, X.; Bai, Y.; Zheng, L.; Liu, M.; Li, Y.; Zhao, R.; Li, Y.; Wu, C. Effect of Different Nitrogen Configurations on Sodium Storage Properties of Carbon Anodes for Sodium Ion Batteries. *ACS Appl. Mater. Interfaces* **2021**, *13*, 56285–56295. [CrossRef] [PubMed]
33. Lin, H.; Miao, W.; Shi, Y.; Mao, G.; Ding, D.; Weng, J.; Fan, Z.; Xu, Q.; Xu, J. N-Doping Activated Presodiation Enhances Sodium-Ion Provision in Hard Carbon Anodes. *Adv. Sci.* **2026**, *13*, e75460. [CrossRef] [PubMed]
34. Yu, Z.; Li, X.; Sun, N.; Chen, H.; Soomro, R.A.; Xu, B. Synergistic regulation of closed pore architecture and interface engineering in hard carbon for high energy density sodium-ion batteries. *Energy Storage Mater.* **2025**, *82*, 104612. [CrossRef]
35. Yabuuchi, N.; Kubota, K.; Dahbi, M.; Komaba, S. Research Development on Sodium-Ion Batteries. *Chem. Rev.* **2014**, *114*, 11636–11682. [CrossRef] [PubMed]
36. Vijaya Kumar Saroja, A.P.; Muruganathan, M.; Muthusamy, K.; Mizuta, H.; Sundara, R. Enhanced Sodium Ion Storage in Interlayer Expanded Multiwall Carbon Nanotubes. *Nano Lett.* **2018**, *18*, 5688–5696. [CrossRef] [PubMed]
37. Chabot, V.; Higgins, D.; Yu, A.; Xiao, X.; Chen, Z.; Zhang, J. A review of graphene and graphene oxide sponge: Material synthesis and applications to energy and the environment. *Energy Environ. Sci.* **2014**, *7*, 1564–1596. [CrossRef]
38. Thommes, M.; Kaneko, K.; Neimark, A.V.; Olivier, J.P.; Rodriguez-Reinoso, F.; Rouquerol, J.; Sing, K.S.W. Physisorption of gases, with special reference to the evaluation of surface area and pore size distribution (IUPAC Technical Report). *Pure Appl. Chem.* **2015**, *87*, 1051–1069. [CrossRef]
39. Li, Z.; Gao, Y.; Luo, W.; Xu, Z.; Wu, J.; Wang, Y.; Zhang, K.; Chen, R.; Lu, Z.; Wang, H.-L. Overcoming the Trade-Off between Initial Coulombic Efficiency and Rate Performance in Hard Carbon Anodes for Sodium-Ion Storage. *ACS Nano* **2026**, *20*, 7589–7600. [CrossRef] [PubMed]
40. Zhao, J.; Liu, X.; Yuan, H.; Feng, S.; Xiong, K.; Xu, X.; Li, Y.; Yang, G. Insights into the microstructure evolution of starch-derived hard carbon for sodium-ion battery. *J. Power Sources* **2025**, *647*, 237367. [CrossRef]
41. Chen, C.; Huang, Y.; Zhu, Y.; Zhang, Z.; Guang, Z.; Meng, Z.; Liu, P. Nonignorable Influence of Oxygen in Hard Carbon for Sodium Ion Storage. *ACS Sustain. Chem. Eng.* **2020**, *8*, 1497–1506. [CrossRef]
42. Li, X.; Zhang, S.; Tang, J.; Yang, J.; Wen, K.; Wang, J.; Wang, P.; Zhou, X.; Zhang, Y. Structural design of biomass-derived hard carbon anode materials for superior sodium storage via increasing crystalline cellulose and closing the open pores. *J. Mater. Chem. A* **2024**, *12*, 21176–21189. [CrossRef]

43. Ai, H.; Qin, J.; Zhou, Q.; Zhou, W.; Xie, J.; Du, K. Tunable Polyethylenimine-Interpenetrated Lignin-Derived Hard Carbons with Enhanced Plateau Capacity for Application in High-Performance Sodium-Ion Batteries. *Ind. Eng. Chem. Res.* **2025**, *64*, 10805–10819. [CrossRef]
44. Sun, D.; Zhao, L.; Sun, P.; Zhao, K.; Sun, Y.; Zhang, Q.; Li, Z.; Ma, Z.; Zheng, F.; Yang, Y.; et al. Rationally Regulating Closed Pore Structures by Pitch Coating to Boost Sodium Storage Performance of Hard Carbon in Low-voltage Platforms. *Adv. Funct. Mater.* **2024**, *34*, 2403642. [CrossRef]
45. Yin, Y.; Tan, Y.; Lu, Y.; Wang, Y.; Yang, J.; Li, Y.; Huang, B. A soft carbon/hard carbon composite synthesized from asphalt/pecan shells as an anode material for sodium-ion batteries. *J. Energy Storage* **2025**, *113*, 115649. [CrossRef]
46. Qiu, Y.; Su, Y.; Jing, X.; Xiong, H.; Weng, D.; Wang, J.-G.; Xu, F.; Wang, H. Rapid Closed Pore Regulation of Biomass-derived Hard Carbons Based on Flash Joule Heating for Enhanced Sodium Ion Storage. *Adv. Funct. Mater.* **2025**, *35*, 2423559. [CrossRef]
47. Nie, W.; Cheng, H.; Liu, X.; Sun, Q.; Tian, F.; Yao, W.; Liang, S.; Lu, X.; Zhou, J. Surface organic nitrogen-doping disordered biomass carbon materials with superior cycle stability in the sodium-ion batteries. *J. Power Sources* **2022**, *522*, 230994. [CrossRef]
48. Zhang, H.; Chen, Z.; Sun, Z.; Cai, M.; Liu, W.; Ye, W.; Gao, H.; Han, J.; Cheng, Y.; Zhang, Q.; et al. Unraveling the Origin of Enhanced K+ Storage of Carbonaceous Anodes Enabled by Nitrogen/Sulfur Co-Doping. *Adv. Funct. Mater.* **2023**, *33*, 2300769. [CrossRef]
49. Wasalathilake, K.C.; Ayoko, G.A.; Yan, C. Effects of heteroatom doping on the performance of graphene in sodium-ion batteries: A density functional theory investigation. *Carbon* **2018**, *140*, 276–285. [CrossRef]
50. Zhao, Y.; Hu, Z.; Fan, C.; Gao, P.; Zhang, R.; Liu, Z.; Liu, J.; Liu, J. Novel Structural Design and Adsorption/Insertion Coordinating Quasi-Metallic Na Storage Mechanism toward High-performance Hard Carbon Anode Derived from Carboxymethyl Cellulose. *Small* **2023**, *19*, 2303296. [CrossRef] [PubMed]
51. Kammoun, H.; Ossonon, B.D.; Tavares, A.C. Nitrogen-Doped Graphene Materials with High Electrical Conductivity Produced by Electrochemical Exfoliation of Graphite Foil. *Nanomaterials* **2024**, *14*, 123. Correction in *Nanomaterials* **2026**, *16*, 318. https://doi.org/10.3390/nano16050318. [CrossRef] [PubMed]
52. Yang, Y.; Liu, C.; Yao, J.; Tang, Z.; Sun, Y.; Zhang, K.; Li, H.; Ma, T.; Qiu, J. Unveiling the role of intrinsic defects in N/S Co-Doped hard carbon for superior sodium-ion batteries. *Chem. Eng. J.* **2025**, *503*, 158441. [CrossRef]
53. Zaman, M.; Alotaibi, B.M.; Jawhari, A.H.; Alyousef, H.A.; Alrowaily, A.W.; Faizan, M.; Ahmad, N. Fabrication and electrochemical investigation of MnCo2O4/PANI nanohybrid for supercapacitor. *J. Sol.-Gel Sci. Technol.* **2025**, *116*, 1464–1476. [CrossRef]
54. Wang, X.; Dong, J.; Ren, J.; Wang, K.; Li, X.; Li, J.; Tao, J. Phosphorus-doped coal-derived hard carbon anodes for high-performance sodium-ion batteries: Synergistic regulation of graphitization and sodium adsorption. *Electrochim. Acta* **2025**, *536*, 146731. [CrossRef]
55. Wang, X.; Hu, Q.; Cui, J.; Hou, J.; Huang, Y.; Liu, X. A Generic Si-Doped Strategy for Hard Carbon Derived from Wuliangye Distillers' Grains to Achieve High-Performance Sodium Ion Batteries. *ACS Appl. Mater. Interfaces* **2025**, *17*, 12004–12013. [CrossRef] [PubMed]
56. Li, S.; Qiu, J.; Lai, C.; Ling, M.; Zhao, H.; Zhang, S. Surface capacitive contributions: Towards high rate anode materials for sodium ion batteries. *Nano Energy* **2015**, *12*, 224–230. [CrossRef]
57. Li, K.; Zhang, J.; Lin, D.; Wang, D.-W.; Li, B.; Lv, W.; Sun, S.; He, Y.-B.; Kang, F.; Yang, Q.-H.; et al. Evolution of the electrochemical interface in sodium ion batteries with ether electrolytes. *Nat. Commun.* **2019**, *10*, 725. Correction in *Nat. Commun.* **2019**, *10*, 1248. https://doi.org/10.1038/s41467-019-09129-6. [CrossRef] [PubMed]
58. Fang, Y.; Lu, M.; Qian, H.; Xiang, J.; Tu, F.; Jiang, Y.; Gan, Y.; He, X.; Huang, H.; Xia, X.; et al. A Cross-Linking Strategy To Regulate the Surface Defects and Pore Structures of Lignin-Derived Hard Carbon as High-Performance Anode for Sodium-Ion Batteries. *ACS Appl. Energy Mater.* **2025**, *8*, 8320–8330. [CrossRef]
59. Ledwoch, D.; Komsiyska, L.; Hammer, E.M.; Smith, K.; Shearing, P.R.; Brett, D.J.L.; Kendrick, E. Determining the electrochemical transport parameters of sodium-ions in hard carbon composite electrodes. *Electrochim. Acta* **2022**, *401*, 139481. [CrossRef]
60. Alvin, S.; Cahyadi, H.S.; Hwang, J.; Chang, W.; Kwak, S.K.; Kim, J. Revealing the Intercalation Mechanisms of Lithium, Sodium, and Potassium in Hard Carbon. *Adv. Energy Mater.* **2020**, *10*, 2000283. [CrossRef]
61. Weppner, W.; Huggins, R.A. Determination of the Kinetic Parameters of Mixed-Conducting Electrodes and Application to the System Li3Sb. *J. Electrochem. Soc.* **1977**, *124*, 1569–1578. [CrossRef]
62. Chen, Y.; Peng, G.; Zhao, M.; Zhou, Y.; Zeng, Y.; He, H.; Zeng, J. Dual-element synergy driven breakthrough in sodium storage performance of phenolic resin-based hard carbon. *Carbon* **2025**, *238*, 120269. [CrossRef]

Disclaimer/Publisher's Note: The statements, opinions and data contained in all publications are solely those of the individual author(s) and contributor(s) and not of MDPI and/or the editor(s). MDPI and/or the editor(s) disclaim responsibility for any injury to people or property resulting from any ideas, methods, instructions or products referred to in the content.